Electronic mobility and crystal structures of 2,5-dimethylanilinium triiodide and tin-based organic-inorganic hybrid compounds

Kamminga, Machteld E.; Gelvez-Rueda, Maria C.; Maheshwari, Sudeep; van Droffelaar, Irene S.; Baas, Jacob; Blake, Graeme R.; Grozema, Ferdinand C.; Paistra, Thomas T. M.

Published in:
Journal of Solid State Chemistry

DOI:
10.1016/j.jssc.2018.12.029

Publication date:
2019

Journal of Solid State Chemistry 270 (2019) 593–600

Contents lists available at ScienceDirect

Journal of Solid State Chemistry

journal homepage: www.elsevier.com/locate/jssc

Electronic mobility and crystal structures of 2,5-dimethylanilinium triiodide and tin-based organic-inorganic hybrid compounds

Machteld E. Kamminga[a,*], María C. Gélvez-Rueda[b], Sudeep Maheshwari[b], Irene S. van Droffelaar[a], Jacob Baas[a], Graeme R. Blake[a], Ferdinand C. Grozema[b], Thomas T.M. Palstra[a,1]

[a] Zernike Institute for Advanced Materials, University of Groningen, Nijenborgh 4, 9747 AG Groningen, the Netherlands
[b] Section Optoelectronic Materials, Department of Chemical Engineering, Delft University of Technology, Van der Maasweg 9, 2629 HZ Delft, the Netherlands

ARTICLE INFO

Keywords:
Organic-organic hybrids
Tin iodide
Triiodide
Hypophosphorous acid
Single-crystal XRD
Microwave conductivity

ABSTRACT

We synthesize single crystals of a new 2,5-dimethylanilinium tin iodide organic-inorganic hybrid compound and 2,5-dimethylanilinium triiodide. Single-crystal X-ray diffraction reveals that the hybrid grows as a unique rhombohedral structure consisting of one-dimensional chains of SnI_6-octahedra that share corners and edges to build up a ribbon along the [111] direction. Notably, we find that hypophosphorous acid, H_3PO_2, is of central importance to the formation of this hybrid. In the absence of H_3PO_2, we synthesize 2,5-dimethylanilinium triiodide from the same starting compounds. We investigate the synthesis routes that drive the growth of these two compounds with distinct crystal structures, appearance and properties. Pulse-radiolysis time-resolved microwave conductivity measurements and density functional theory calculations reveal that both compounds have low charge carrier mobilities and very long lifetimes, consistent with their one-dimensional structural characteristics. Our findings give a better understanding of the relation between synthesis, crystal structures and charge carrier mobilities.

1. Introduction

Organic-inorganic hybrid perovskites, such as $CH_3NH_3PbI_3$, have attracted growing attention as promising candidates for diverse optoelectronic applications. The combination of organic and inorganic components in a single compound leads to a class of materials that exhibit a large variety of properties. Because of their unique optical [1,2] and excitonic [3,4] properties and electrical [5] and ionic conductivity [6], various optoelectronic applications are reported in the literature. These applications include light-emitting diodes [7,8], lasers [9,10], photodetectors [11] and efficient planar heterojunction solar cell devices [12–16]. However, the best performing organic-inorganic hybrid solar cells are lead-based. Substitution of lead is desired because of its toxicity [17]. The feasibility of substituting tin for lead has been studied [18–21], because they are in the same group in the periodic table and they are isoelectronic in terms of their valence shell and both have a lone pair of electrons. However, tin has the major disadvantage that Sn^{2+} can oxidize easily to Sn^{4+}. Still, tin-based hybrid perovskites are reported to have excellent mobilities in transistors [22] and can be intentionally or unintentionally doped to become metallic [23,24]. Furthermore, encapsulation under inert atmosphere allows for the successful implementation and study of tin-based perovskite solar cell devices [18,19].

In this work, we synthesize single crystals of a new tin-based hybrid compound: 2,5-dimethylaniline (abbreviated as 2,5-DMA) tin iodide (2,5-$DMASnI_3$). The motivation for synthesizing this compound is that tin-based compounds generally exhibit good mobilities and that the introduction of aromatic 2,5-DMA molecules might enhance the mobility due to possible π-π stacking. Moreover, the aromaticity of the organic cations can benefit the crystal growth. Using single-crystal X-ray diffraction, we find that 2,5-$DMASnI_3$ grows as a unique rhombohedral structure, consisting of one-dimensional (1D) chains of SnI_6-octahedra that share corners and edges to build up a ribbon along the [111] direction. Various low-dimensional tin-based hybrid structures have previously been reported [25]. However, the structural motif of 2,5-$DMASnI_3$ is of an hitherto unknown type.

In addition to the target product, 2,5-$DMASnI_3$, we also synthesized single crystals of another new compound: 2,5-$DMAI_3$. This triiodide

* Corresponding author.
E-mail address: m.e.kamminga@rug.nl (M.E. Kamminga).
[1] Present address: University of Twente, the Netherlands.

https://doi.org/10.1016/j.jssc.2018.12.029
Received 1 November 2018; Received in revised form 10 December 2018; Accepted 16 December 2018
Available online 18 December 2018

salt forms a monoclinic structure consisting of linear I_3^- units, separated by the organic amines. We find that both compounds, 2,5-DMASnI$_3$ and 2,5-DMAI$_3$, form from the same starting compounds. However, the product depends on the experimental conditions and more specifically, on the presence of H_3PO_2. Pulse-radiolysis time-resolved microwave conductivity measurements and density functional theory calculations reveal that the charge transport in both compounds is limited to the SnI_6-ribbons and I_3^- units. This one-dimensional (1D) confinement enlarges the effective mass of the charge carriers. While their mobilities are relatively low, the charge carrier lifetimes are lengthened by the more ionic character of the 1D units, as observed in 2,5-DMAI$_3$. Our findings provide a better understanding of the relation between synthesis, crystal structures and charge carrier mobilities.

2. Materials and methods

2.1. Crystal growth of 2,5-dimethylanilinium tin iodide

Single crystals of 2,5-dimethylanilinium tin iodide (2,5-DMASnI$_3$) were grown following the method previously reported by Stoumpos et al. to synthesize methylammonium tin iodide and formamidinium tin iodide [20]. First, the 2,5-dimethyliodide salt (2,5-DMAI) was synthesized from an equimolar mixture of 2,5-DMA and HI. A syringe was used to slowly add concentrated (57 wt%) aqueous hydriodic acid (Sigma Aldrich; 99.95%) to 2,5-DMA (Sigma Aldrich; 99%). The mixture was heated to 70 °C to remove excess solvent. The resulting white salt was washed with diethyl ether (Avantor) and dried in air. Subsequently, a 100 mL 3-necked Schlenk flask was charged with 6.8 mL concentrated (57 wt%) aqueous hydriodic acid (Sigma Aldrich; 99.95%) and 1.7 mL concentrated (50 wt%) aqueous hypophosphorous acid, H_3PO_2 (Sigma Aldrich). This mixture was degassed with argon and kept under an argon atmosphere throughout the experiment. 373 mg (1 mmol) SnI_2 (Sigma Aldrich; 99%) was added to the flask and dissolved upon heating the mixture to 120 °C using an oil bath, while stirring magnetically. A yellow mixture was obtained. A stoichiometric amount of 1 mmol of the 2,5-DMAI salt was added to the hot solution and dissolved immediately. Next, the solution was slowly evaporated at 120 °C to approximately half its original volume while stirred continuously. Stirring was then discontinued and the mixture was left to cool down to room temperature at a rate of approximately 20 °C/hour. Upon cooling, crystals shaped as *yellow needles* with a length of approximately 3 mm were obtained. In the rest of this work, this synthesis method is referred to as the *Stoumpos method*.

2.2. Crystal growth of 2,5-dimethylanilinium triiodide

Single crystals of 2,5-dimethylanilinium triiodide (2,5-DMAI$_3$) were grown at room temperature, following a modified layered-solution synthesis method previously reported by Mitzi [26]. In this method, 60 mg (0.16 mmol) SnI_2 (Sigma Aldrich; 99%) was added to 3.0 mL of concentrated (57 wt%) aqueous hydriodic acid (Sigma Aldrich; 99.95%). The SnI_2 did not fully dissolve, and only the solution was transferred into a standard size (18 × 150 mm) glass test tube. 3.0 mL of absolute MeOH (Lab-Scan, 99.8%) was carefully placed on top of the red-brown SnI_2/HI mixture, without mixing the solutions. A sharp interface was formed between the two layers due to a large difference in densities. 2,5-DMA (Sigma Aldrich; 99%) was added in great excess by adding 15 droplets, using a glass pipette. The test tube was covered with aluminum foil and kept in a fume hood under ambient conditions. This method turned out to be very slow. It took more than a month to grow black/red bar-shaped crystals of up to 3 mm long. Moreover, as we observed that tin was not included in the final product (2,5-DMAI$_3$ was the product formed), we found that this elaborate method was not necessary. Simply adding MeOH and 2,5-DMA to the filtered SnI_2/HI mixture, briefly stirring and leaving it in the fume hood under ambient conditions gave the same result. However, using this simplified method, crystals were observed within 24 h. This led us to believe that the evaporation rate was the most important parameter for obtaining this product. Note that the addition of MeOH is not vital to the formation of 2,5-DMASnI$_3$. It does promote the solubility of the organic component, as it prevents the formation of 2,5-DMAI, necessary to form 2,5-DMAI$_3$. However, the absence of MeOH reduced the evaporation rate, and subsequently, larger crystals of up to around 8 mm long were obtained. While we modified the synthesis method from the original method designed by Mitzi [26], in the rest of this work we still refer to this simplified method as the *Mitzi method*.

2.3. Single-crystal X-ray diffraction

Single-crystal X-ray diffraction (XRD) measurements were performed using a Bruker D8 Venture diffractometer equipped with a Triumph monochromator and a Photon100 area detector, operating with Mo Kα radiation (0.71073 Å). A 0.3 mm nylon loop and cryo-oil were used to mount the crystals. The crystals were cooled with a nitrogen flow from an Oxford Cryosystems Cryostream Plus. Data processing was done using the Bruker Apex III software and the SHELX97 [27] software was used for structure solution and refinement. Full-matrix least squares refinement against F^2 was carried out using anisotropic displacement parameters. Multi-scan absorption corrections were performed. Hydrogen atoms were added by assuming a regular tetrahedral coordination to carbon and nitrogen, with equal bond angles and fixed distances.

2.4. Pulse-radiolysis time-resolved microwave conductivity

Charges were generated in the materials by ionization using short pulses (5–20 ns) of high energy electrons (3 MeV) from a Van de Graaff accelerator. In this technique, charge carriers are generated by irradiation with a short pulse of high-energy electrons (3 MeV). Subsequently, the change in power ($\Delta P(t)$) of high frequency microwaves reflected by the microwave cell is monitored to determine the change in conductivity ($\Delta\sigma(t)$) of the material. The mobility of the charge carriers (μ) can be derived if their initial concentration ($N_p(0)$) is known, according to Eq. (1). In addition, the recombination mechanisms are studied by varying the initial concentration of charge carriers by varying the length of the high-energy electron pulse.

$$\frac{\Delta P(0)}{P} = A\Delta\sigma(0) = \mathrm{A}e\sum N_p(0)\mu \quad (1)$$

The change in conductivity in the samples was monitored using microwaves in a frequency range from 28 to 38 GHz. The crystals, as synthesized, were placed in a polyether ether ketone (PEEK) holder with a cavity of 6 × 3 × 2 mm^3. The PEEK block with the sample was placed inside a rectangular waveguide copper cell of 14 mm in length, with a 7.1 × 3.55 mm^2 front side. The copper cell was mounted in a cryostat in which the temperature can be varied between 150 and 400 K.

2.5. Density functional theory calculations

The band structures of both crystals were computed at the density functional theory (DFT) level of theory using VASP 5.4.1. The calculations were performed using the projector augmented wave (PAW) pseudopotentials [28,29] with the van-der-Waals-corrected [30] PBE exchange correlation functional [31,32]. The energy cutoff for the charge density calculations was 500 eV and a Gamma centered K-point grid with dimensions of 4 × 4 × 4 was chosen. A denser K-point grid of 210 K-point along the high-symmetry points in the brillouin zone was used for the band structure calculations.

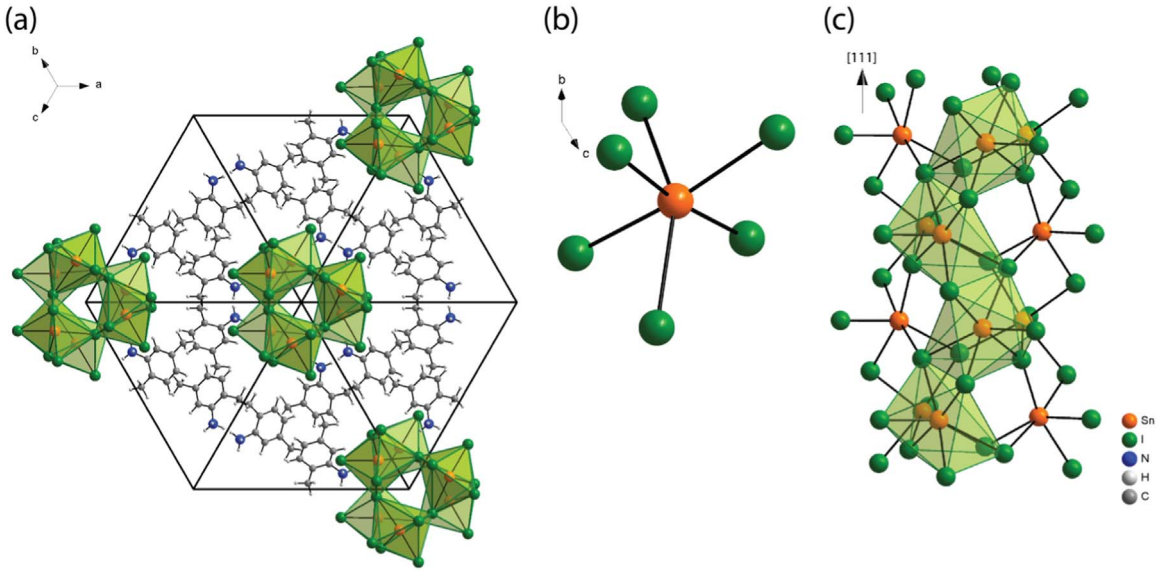

Fig. 1. Crystal structure of 2,5-DMASnI$_3$. (a) Polyhedral model of the full crystal structure, projected along the [111] direction. (b) A single SnI$_6$-octahedron, showing severe distortion. (c) A single inorganic ribbon. Shading represents the strip of SnI$_6$-octahedra that share edges. The total inorganic ribbon consists of three such edge-sharing strips that are connected through corner-sharing.

3. Results and discussion

We explored two different methods to synthesize 2,5-DMASnI$_3$ (2,5-DMA=2,5-dimethylaniline) and we found that the two techniques gave rise to different products. Using the *Stoumpos method*, we obtained the tin-based organic-inorganic hybrid, 2,5-DMASnI$_3$, in the form of yellow needles. With the *Mitzi method*, we obtained the triiodide salt 2,5-DMAI$_3$ as very dark red/black bar-shaped crystals. No tin was observed in this structure. We used single-crystal XRD to study both structures in detail. Moreover, we studied the reaction parameters of both methods to understand what drives the formation of one compound over the other. This will be discussed below. First, both crystal structures are described (see Figs. 1 and 2). Crystallographic and refinement parameters of both compounds are listed in Table 1.

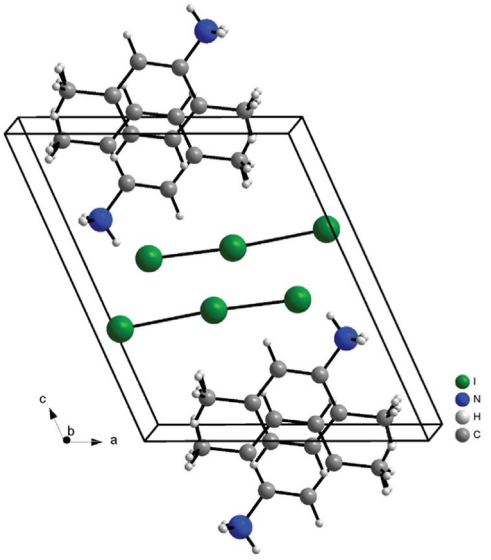

Fig. 2. Crystal structure of 2,5-DMAI$_3$. The hydrogen atoms of the methyl groups are split over two positions by symmetry and should be considered illustrative only.

Table 1
Crystallographic and refinement parameters of 2,5-DMAI$_3$ and 2,5-DMASnI$_3$.

	2,5-DMAI$_3$	**2,5-DMASnI$_3$**
Temperature (K)	100(2)	100(2)
Formula	$C_8H_{12}I_3N$	$C_8H_{12}I_3NSn$
Formula weight (g/mol)	502.89	621.58
Crystal size (mm^3)	0.08 × 0.10 × 0.16	0.02 × 0.06 × 0.22
Crystal color	Black/dark red	Yellow
Crystal system	Monoclinic	Rhombohedral
Space group	$P2_1/m$ (no. 11)	$R3c$ (no. 161)
Symmetry	Centrosymmetric	Non-centrosymmetric (polar)
Z	2	6
D (calculated) (g/cm^3)	2.686	2.900
F(000)	452	2208
a (Å)	9.3195(8)	17.2991(9)
b (Å)	6.6052(6)	17.2991(9)
c (Å)	11.0657(9)	17.2991(9)
α (°)	90.0	117.373(2)
β (°)	114.095(3)	117.373(2)
γ (°)	90.0	117.373(2)
Volume (Å^3)	621.82(9)	2143.5(4)
μ (mm^{-1})	7.497	8.980
Min/max transmission	0.380/0.585	0.196/0.810
θ range (degrees)	3.08–36.39	2.76–27.22
Index ranges	−13 < h < 13	−24 < h < 24
	−9 < k < 9	−24 < k < 24
	−15 < l < 15	−24 < l < 24
Data/restraints/parameters	2051/0/76	4367/1/110
GooF of F^2	1.195	1.200
No. total reflections	28,187	113,765
No. unique reflections	2051	4367
No. obs Fo > 4σ(Fo)	1983	3746
R_1 [Fo > 4σ(Fo)]	0.0197	0.0494
R_1 [all data]	0.0205	0.0683
wR_2 [Fo > 4σ(Fo)]	0.0512	0.1128
wR_2 [all data]	0.0518	0.1347
Largest peak and hole (e Å^3)	0.48 and −2.71	1.61 and −1.76

3.1. 2,5-DMASnI$_3$

Fig. 1 shows the crystal structure of 2,5-DMASnI$_3$. As listed in Table 1, structural refinement was performed in the polar space group *R3c*, using the rhombohedral setting. The combination of single-crystal XRD measurements at 100 K and 300 K, and differential scanning calorimetry (DSC) and thermogravimetric analysis (TGA) above room

Table 2
Appearance, I1-I2-I3 angle and presence of π-π interactions for selected triiodide salts containing an organic cation.

Organic cation	Appearance	I1-I2-I3 angle (°)	π–π interaction[a]
2,5-dimethylanilinium	Red/black bar	175.989(2)	Yes, 3.303 Å
2-aminopyridin-1-ium [45]	Orange plate	176.017(9)	Yes, 3.423 Å
(*E*)–2-[4-(dimethylamino)styryl]–1]methylpyridinium) [46]	Orange needle	180.0	Yes, 3.306 Å
4-(4-pyridyl)pyridinium [47]	Yellow/brown prism	176.443(13)	Yes, 3.759 Å
Trans–4-[*p*-(*N*,*N*-diethylamino)styryl]-*N*-methylpyridinium [48]	Dark red prism	177.50(2)	Yes, 3.585 Å
4-*tert*-butylpyridinium [49]	Red block	177.55(3)	No
1,3-bis(2,6-diisopropylphenyl)–4,5-dihydro-1*H*-imidazol-3-ium [50]	Brown block	178.309(18)	No
1,4-dimethylpyridinium [51]	Brown plate	180.0	No
6,6,9,9-tetramethyl-1,2,5,6,9,9a-hexahydroimidazo[2,1-*d*][1,2,5]dithiazepin-1-ium] [52]	Brown prism	178.05(4)	No
dihydrobis(methylamine)borate [53]	Red/purple needle	179.232(15)	No
2-(2-pyridyl)pyridinium [41]	Brown needle	177.88(5)	No
1-ethylpyridinium [42]	Red/black block	177.70(2)	No
1,2,4-trimethylpyridinium [42]	Red/black block	179.76(2)	No
1,2,3,5-tetramethyl-1*H*-pyrazol-2-ium [54]	Red prism	177.099(12)	No
2,5-dibromopyrazinium [55]	Yellow block	180.0	No

[a] Distance between the planes of the aromatic rings.

temperature, revealed that no phase transitions take place before decomposition at around 350 K.

While 2,5-DMASnI$_3$ has the same structural formula as the cubic ABX$_3$ hybrid perovskite structure, with A the monovalent organic cation, B the divalent metal and X the halide, the structural motif is very different. As shown in Fig. 1(a), the structure of 2,5-DMASnI$_3$ consists of SnI$_6$-octahedra that form 1D chains along the [111] direction. This 1D nature is also apparent from the shape of the crystals. The crystals grow as needles and the longest direction corresponds to the [111] direction. As shown in Fig. 1(b), the SnI$_6$-octahedra are strongly distorted. The three I-Sn-I angles deviate from a perfect 180°, with values of 171.019(1)°, 166.243(1)° and 154.760(1)°, respectively. We believe that this distortion is caused by the interaction of the NH_3^+ group with the iodide pairs and indirectly affect the distortion of the SnI$_6$-units via the Sn^{2+} lone pair. Fig. 1(c) shows a single inorganic ribbon. Each ribbon consists of three strips of edge-sharing SnI$_6$-octahedra that are connected to each other by corner-sharing. This bonding pattern is rather unusual and we have not encountered this in any tin-based hybrid structure reported in the literature. The organic molecules form a herringbone-type structure. Therefore, no π-π stacking is observed. The ammonium groups are oriented towards the inorganic ribbons, to create hydrogen bonding.

If charge transfer would occur through both the organic and inorganic components, we believe that the polar nature of the structure (space group *R3c*) might aid charge separation. However, we also argue that the band gap is quite large as the crystals are yellow in color. Moreover, our previous work on lead iodide-based hybrids has shown that the dimensionality and connectivity of the metal halide octahedra plays a significant role in determining the band gap of the compound [33]. The 1D nature and presence of edge-sharing SnI$_6$-octahedra in 2,5-DMASnI$_3$ then contribute to the large band gap. As shown below, our DFT calculations estimate the band gap to be 2.37 eV.

3.2. 2,5-DMAI3

Fig. 2 shows the crystal structure of 2,5-DMAI$_3$. As listed in Table 1, refinement was performed in the monoclinic space group $P2_1/m$. Single-crystal XRD measurements at 100 K and 300 K, and DSC and TGA above room temperature, revealed that no phase transitions take place in 2,5-DMAI$_3$, before decomposition at around 410 K. 2,5-DMAI$_3$ is a triiodide salt, and while SnI$_2$ was one of the starting compounds, no tin was observed in the product. We used energy-dispersive X-ray spectroscopy (EDAX) measurements to prove the absence of tin. As shown in Fig. 2, the triiodide ions are (nearly) linear and isolated from each other. Triiodide ions can be divided into two types: asymmetric and symmetric. Symmetric and linearly shaped triiodide ions are often found in charge transfer complexes, such as the organic superconductor β-(BEDT-TTF)$_2$I$_3$ which has linear I_3^- ions at an inversion center [34,35]. In 2,5-DMAI$_3$, the anions are highly asymmetric: the I1-I2 and I2-I3 distances are 3.1373(4) Å and 2.779(3) Å, respectively. This large asymmetry means that the I_3^- unit exhibits strong ionic character. Furthermore, the triiodide ion deviates significantly from linearity with an I1-I2-I3 angle of 175.989(2)°, which is close to the mean value for triiodide ions taken from the Crystallographic Open Database (COD) of 178° (see Table 2) [36–40]. Moreover, linear and symmetrical I_3^- ions are generally associated with large cations, in contrast to the asymmetric bent I_3^- anions found with small asymmetric or highly charged cations [41]. Notably, all organic molecules lie parallel to the (101)-plane and hence, parallel to each other. The distance between two 2,5-DMA molecules corresponds to half a unit cell, i.e. 3.3026(6) Å. The molecules are stacked in an off-set manner, but there is nevertheless a degree of π–π overlap between adjacent rings.

There are several triiodide salts reported in literature, some of which are listed in Table 2. This list is not complete, but based on all structures found in the Crystallographic Open Database (COD) except for the 1-ethylpyridinium and 1,2,4-trimethylpyridinium salts, for which no crystallographic information files (CIFs) were deposited in the database. However, since these two organic molecules have a similar size to 2,5-DMA, we manually constructed CIFs from the structural data presented in the papers [42]. Note that we only considered fully organic cations. Cations containing for example iron or arsenic are excluded from this list [43,44]. Almost all triiodide salts found in the COD are published as structure reports. The triiodide salts are often reported as undesired byproducts instead of a target product. We discuss below which experimental conditions influence the growth of both the triiodide salt and the target product, 2,5-DMASnI$_3$, adding to the understanding of why triiodide salts can form under certain conditions. Furthermore, as most triiodide salts are reported as structure reports, not much has been said about their properties. As shown in Table 2, a few of these compounds have π-π stacking and the compound we present here is one of these. Note that the π-π interaction distance is defined as the distance between the planes of adjacent rings, along the stacking direction. This means that any off-set stacking is ignored. The combination of the dark color (See Fig. 3(a)) and π–π stacking in our structure led us to believe that the electrical conductivity could be large. However, the ionic character of the I_3^- unit might reduce the conductivity due to limited charge transfer between neighboring I_3^- units. Investigation of the carrier mobilities and a theoretical analysis are discussed below.

As stated above, the formation of either 2,5-DMASnI$_3$ or 2,5-DMAI$_3$ directly depends on the synthesis method used. In Table 3 we list the differences in experimental conditions between

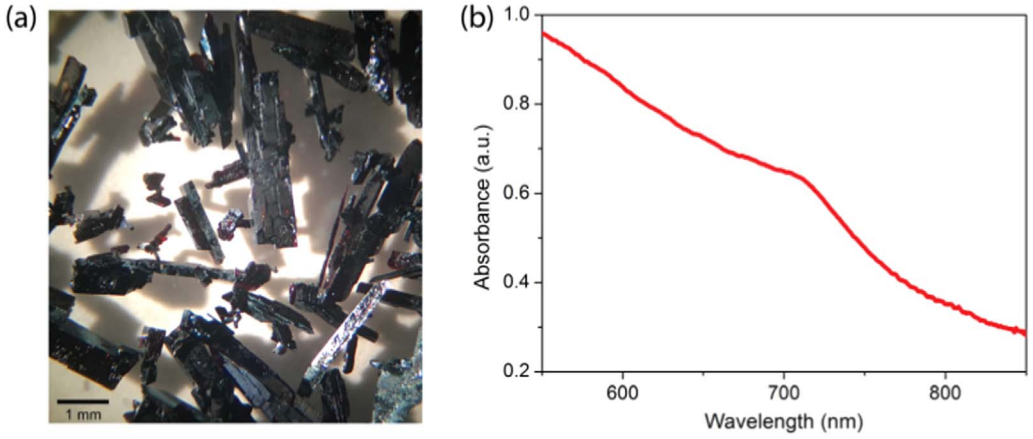

Fig. 3. (a) Photograph of 2,5-DMAI$_3$ single crystals. (b) Absorption spectrum of 2,5-DMAI$_3$ single crystal, showing excitonic absorption at around 720 nm.

Table 3
Comparison of synthesis parameters used in both synthesis methods.

	Stoumpos method [20]	*Mitzi method* [26]
Temperature	120 °C	25 °C
State of organic precursor	2,5-DMAI (s)	2,5-DMA (l)
Solvents	HI and H_3PO_2	HI (and MeOH)
Atmosphere	Argon	Ambient
Obtained compound	2,5-DMASnI$_3$	2,5-DMAI$_3$

the two methods. To understand which difference induces the different products, we investigate the effect of all experimental conditions: temperature, state of organic precursor, solvent and atmosphere.

3.3. Effect of temperature

We grew 2,5-DMAI$_3$ at room temperature, while we grew 2,5-DMASnI$_3$ at elevated temperature. To investigate the effect of temperature, we performed both synthesis methods at the opposite temperatures. The *Mitzi method* appears to be successful at 120 °C. The same product was obtained. However, the crystals contained more imperfections and were smaller in size. We reason that this is caused by the rapid evaporation rate at 120 °C, which negatively influences the crystal quality. This is a similar argument to the necessity of adding MeOH to the reaction mixture to slow the evaporation rate as discussed in the Materials and Methods. Conversely, the *Stoumpos method* does not work at room temperature. The main problem here is that the relatively large amount of SnI_2 does not fully dissolve at room temperature, and only crystals of SnI_2 were obtained. Possibly, the optimal relative concentrations of organic and inorganic components were not reached or the hybrid did not nucleate due to the relatively easy growth of existing SnI_2 particles. Furthermore, we dissolved both products in EtOH and allowed them to recrystallize at ambient conditions. This appeared to be successful for both 2,5-DMAI$_3$ and 2,5-DMASnI$_3$. Consequently, both products are stable and the driving force for formation of either of the two components lies in the initial formation of the product. Thus, we find that the elevated temperature is important for the growth of 2,5-DMASnI$_3$, but as 2,5-DMAI$_3$ can also form at the same temperature, this is not the crucial difference between the two methods.

3.4. Effect of the state of the organic precursor

In the *Stoumpos method*, 2,5-DMA is added as a pre-made 2,5-DMAI salt, while in the *Mitzi method*, 2,5-DMA is directly used. Here we explored the necessity of forming the 2,5-DMAI salt before continuation of the synthesis process. We found that this step can be removed from the synthesis procedure. The salt immediately dissolves in HI, and adding the salt instead of the solution, only adds more iodine to the reaction mixture, while there is already a great excess of HI. For the *Mitzi method*, the use of the pre-made 2,5-DMAI salt, instead of 2,5-DMA as a solution, also did not influence the product formed. This method is also based on an excess of HI, therefore no change is observed. Thus, the state of the organic component does not influence the formation of the final product in either of the synthesis methods.

3.5. Effect of atmosphere and hypophosphorous acid

Despite the fact that both 2,5-DMAI$_3$ and 2,5-DMASnI$_3$ are stable in air for at least 24 h, both synthesis methods are performed under different environmental conditions. The *Stoumpos method* is performed under inert atmosphere, while the *Mitzi method* is performed under ambient conditions. Notably, when the opposite type of atmosphere was used, both synthesis methods failed. The *Stoumpos method* failed in ambient atmosphere, as no 2,5-DMASnI$_3$ was formed. The *Mitzi method* also failed to give any product under inert environment. However, when the reaction mixture was exposed to air, 2,5-DMAI$_3$ formed within one hour. This leads to the conclusion that oxygen plays a crucial role in the formation of the triiodide salt. While Sn^{2+} easily oxidizes to Sn^{4+}, neither was observed in the final product 2,5-DMAI$_3$. Notably, HI is also not very stable in air. The iodide ions, I^-, can be oxidized to iodine, I_2. This is the reason why H_3PO_2 should be introduced [56]. H_3PO_2 is a reducing agent that reduces I_2 back to I^-. Consequently, 2,5-DMASnI$_3$ can be formed with the *Stoumpos method*. In the case of the *Mitzi method*, the presence of ambient air and lack of any reducing agent oxidizes a significant amount of I^- to I_2, which in turn reacts with I^- to form the triiodide complex: I_3^-. This triiodide easily combines with the organic component to form the triiodide salt, 2,5-DMAI$_3$. Thus, the addition of H_3PO_2 is crucial for the synthesis of the 2,5-DMASnI$_3$ hybrid. However, H_3PO_2 is not the only experimental requirement for the synthesis of the hybrid; as stated above, the reaction temperature is also crucial. Additional experiments showed that adding H_3PO_2 to the reaction mixture used in the *Mitzi method* (25 vol%) still produced 2,5-DMAI$_3$ when exposed to air. The main difference is that it took significantly longer to grow the crystals. Thus, in order to grow the 2,5-DMASnI$_3$ hybrid, H_3PO_2, inert atmosphere and elevated temperatures are required. Leaving out any of these three conditions prevents the desired product from forming or gives 2,5-DMAI$_3$. In order to grow 2,5-DMAI$_3$, the key experimental condition is the absence of inert atmosphere.

Peculiar to the *Mitzi method* is the fact that no triiodide salt forms when different organic molecules are used. We have tried this method with several organic moieties, including benzylammonium and 2-thiophenemethylammonium, but none gave any product. As shown in Table 2, several organic triiodide salts have been successfully made,

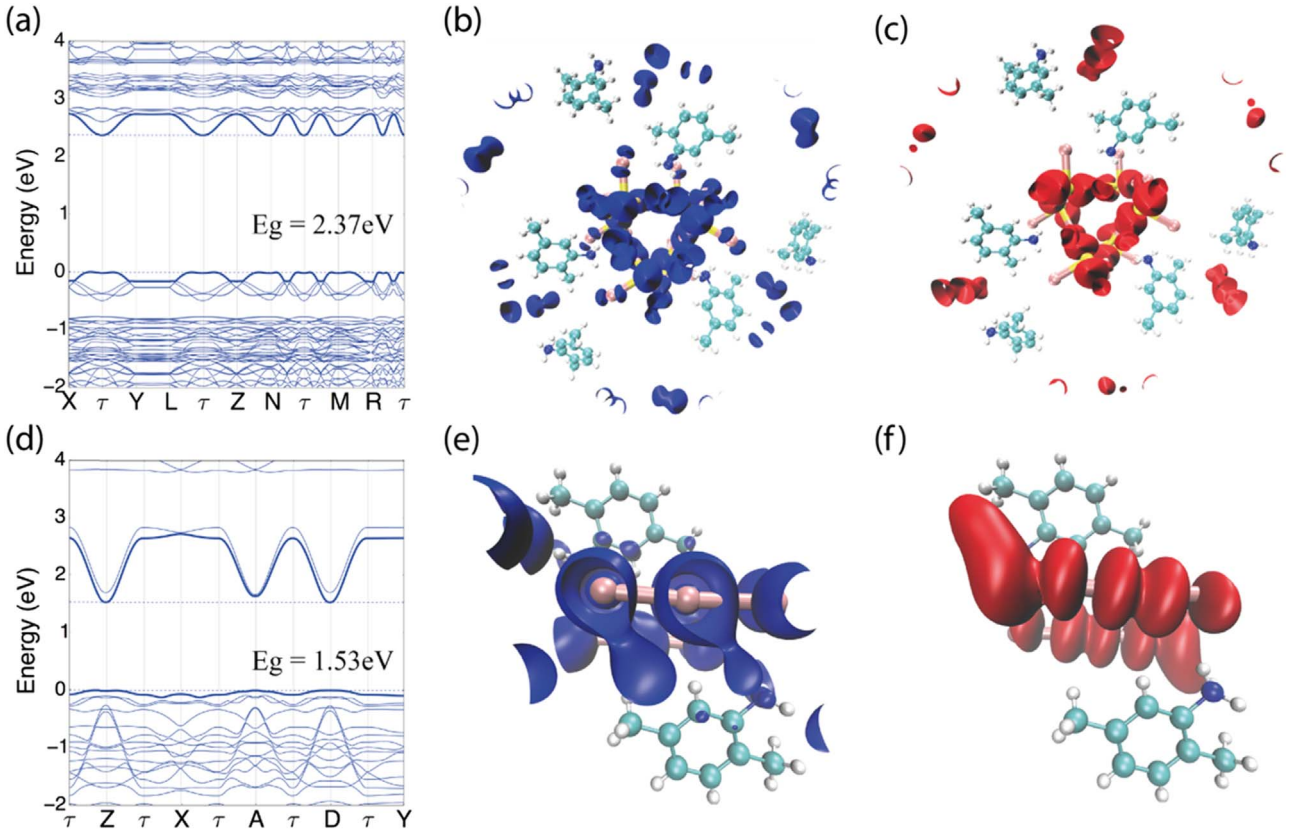

Fig. 4. DFT band structure calculations and charge densities at the bottom of the conduction band and the top of the valance band for 2,5-DMASnI$_3$ (a, b and c) and 2,5-DMAI$_3$ (d, e and f).

but we believe that it is not possible to form salts with every organic cation. We believe that 2,5-DMA has a more favorable size and shape for inclusion in a triiodide salt. While benzylammonium and 2-thiophenemethylammonium have a relatively long shape with respect to the ammonium group, 2,5-DMA has a wider shape. Furthermore, the widest span in 2,5-DMA is between the two methyl groups and corresponds to 5.8545(3) Å. Notably, the span of the I_3^- complex in 2,5-DMAI$_3$ is 5.9088(3) Å, which is very similar. We believe that the growth of 2,5-DMAI$_3$ is favorable compared to some other XI$_3$ salts, with X being an organic cation, as both building blocks are similar in size.

As shown in Table 2, the appearance of 2,5-DMAI$_3$ is rather dark, indicating a relatively small band gap. The absorption spectrum is shown in Fig. 3(b). The spectrum appears to show some excitonic absorption at around 720 nm. As shown below, our DFT calculations estimate the band gap to be 1.53 eV, in close agreement with Fig. 3(b). While we argue that the experimental band gap will be of the order of 1.55 eV, it is difficult to extract the exact band gap due to absorbance that extends beyond 1.55 eV (800 nm). Notably, no emission could be detected. However, Fig. 4(d) indicates a direct band gap in this material.

In order to clarify the electronic properties of these materials, we performed DFT band structure calculations. 2,5-DMASnI$_3$ has an indirect band gap and 2,5-DMAI$_3$ has a direct band gap at the D point. Moreover, we found that the effective mass of the charge carriers in these materials is one to two orders of magnitude larger than for 3D and 2D perovskites (see Fig. 4 and Table 4) [57–59]. This is in agreement with our experimental results. We attribute these lower charge carrier mobilities to the distortions in the structure that reduce the dimensionality of charge transport by creating 1D fragments. In 2,5-DMASnI$_3$, clear 1D pathways are formed by the corner- and edge-sharing of SnI$_6$-octahedra. Bader charges were calculated for the I_3^- units and the organic cations and we found that the I_3^- unit has a charge of −0.76 and the organic cation has a charge of +0.76. This indicates the pure ionicity of the compound. In 2,5-DMAI$_3$, alternating 1D columns of I_3^- and DMA can be identified. For both compounds, this 1D confinement leads to higher effective masses of the charge carriers and hence a lower mobility [57–59]. The charge densities at the top of the valence band and the bottom of the conduction band for both compounds are shown in Fig. 4. 2,5-DMASnI$_3$ has both the top of the valence band and bottom of the conduction band on the π-orbitals of the Sn and I atoms. 2,5-DMAI$_3$ has both the top of the valence band and bottom of the conduction band on the π-orbitals of the I atoms. It is clear that for both 2,5-DMASnI$_3$ and 2,5-DMAI$_3$, these bands are restricted to a one-dimensional region of the crystal. In 2,5-DMASnI$_3$, both the valence and the conduction band are located at the Sn and I atoms, while for 2,5-DMAI$_3$, both bands are on the columns consisting of I_3^- ions. The effective mass depends on how the orbitals combine to result in a band. The coupling in the case of the 2,5-DMAI$_3$ valence band can be regarded as fairly inefficient due to the decoupled orbitals of iodide, whereas in the case of the 2,5-DMASnI$_3$ valence band the coupling is more dominant and the orbitals are not decoupled. This explains why the hole effective mass is lower in the

Table 4
Band gap, band width and effective mass of charge carriers at the top of the valence band and bottom of the conduction band for 2,5-DMASnI$_3$ and 2,5-DMAI$_3$. The effective masses for 2,5-DMASnI$_3$ are calculated at the Gamma point (0, 0, 0) between X and Y. The effective masses for 2,5-DMAI$_3$ are calculated at the D point (0.5, 0, 0.5).

	2,5-DMASnI$_3$	**2,5-DMAI$_3$**
Band gap (eV)	2.37	1.53
HOMO (eV)	0.16	0.12
LUMO (eV)	0.37	1.19
Hole effective mass (m*)	0.12	60.88
Electron effective mass (m*)	1.06	0.59

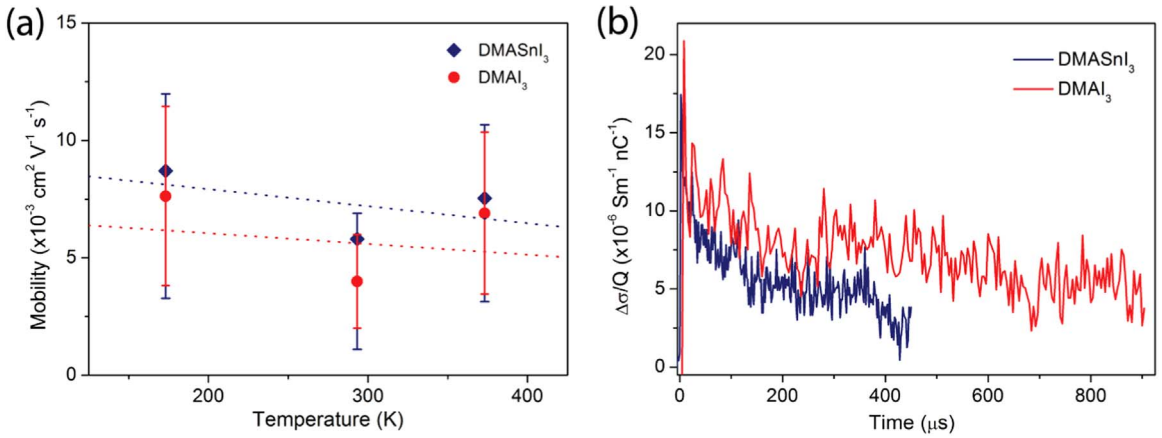

Fig. 5. (a) Mobility of 2,5-DMASnI$_3$ and 2,5-DMAI$_3$ as a function of temperature. Error bars are defined as 50% of the base value. Dotted lines are drawn to guide the eye. (b) Change in conductivity of as 2,5-DMASnI$_3$ and 2,5-DMAI$_3$ a function of time, measured at room temperature.

case of 2,5-DMASnI$_3$ compared to 2,5-DMAI$_3$. The electron effective masses are given by the conduction band, which has a high coupling as seen in the charge density plots of Fig. 4. Thus, the electron effective masses of both compounds are of the same order of magnitude. The low dimensionality is also reflected by the band curvature in different directions. For directions perpendicular to the 1D pathway, the effective mass is much larger than along these pathways.

To study the mobility and recombination mechanisms of charge carriers in both 2,5-DMASnI$_3$ and 2,5-DMAI$_3$, we performed pulse-radiolysis microwave conductivity measurements (PR-TRMC) [60,61]. Fig. 5(a) shows the mobility of 2,5-DMASnI$_3$ and 2,5-DMAI$_3$ as a function of temperature. The mobilities for both compounds are very similar at room temperature, 0.006 cm^2 V^{-1} s^{-1} and 0.004 cm^2 V^{-1} s^{-1}, respectively, and fall within the same error margin. Moreover, the values do not change significantly at higher or lower temperatures. Notably, these values are three orders of magnitude lower than the values measured with the same technique for three-dimensional hybrid perovskites, such as $CH_3NH_3PbI_3$ (~1.5 cm^2 V^{-1} s^{-1}) [58,59], and two orders of magnitude lower than for two-dimensional hybrids, such as $[CH_3(CH_2)_3NH_3]_2PbI_4$ (~0.3 cm^2 V^{-1} s^{-1}) [57]. These results are in agreement with our DFT calculations, as the charge carrier mobility is inversely proportional to the effective mass. We believe that these lower mobilities are caused by the large distortions in the structure of the materials that introduce 1D structural fragments.

The change in conductivity as a function of time is shown in Fig. 5(b). The lifetime of the charge carriers is very long for both compounds: approximately 400 μs for 2,5-DMASnI$_3$ and 1 ms for 2,5-DMAI$_3$. These long lifetimes are caused by the nature of the experiment and the structure of the materials. During PR-TRMC measurements, the electron pulse ionizes the charge carriers with a high energy (20 eV per ionization event on average) [60,61]. Consequently, the electrons and holes are generated far away from each other. Considering the structure of both compounds, the electrons and holes are most likely generated in different 1D ribbons of SnI_6-octahedra in 2,5-DMASnI$_3$ and in different I_3^- units in 2,5-DMAI$_3$. The 1D confinement and large effective masses in the perpendicular direction results in slow recombination and very long carrier lifetimes. The longer lifetime of 2,5-DMAI$_3$, compared to 2,5-DMASnI$_3$, is possibly related to the high ionic character of the I_3^- units, which aids charge separation. To study the lifetime when the charge carriers are generated close to each other, we performed photoconductivity TRMC measurements with laser excitation [57]. However, we did not obtain any photoconductivity signal. By definition, these measurements yield the product of the mobility and charge dissociation [57]. From the PR-TRMC measurements, it is clear that the charge carriers are mobile. Thus, the absence of a photoconductivity signal means that the charge carriers do not dissociate or recombine very quickly due to a high exciton binding energy. We conclude that the exciton binding energy is probably very large in these materials, as a result of the strong 1D confinement in both materials. This is consistent with previous measurements on 2D perovskite structures where much lower photoconductivity was measured, combined with very short carrier lifetimes [57].

4. Conclusion

In conclusion, we have synthesized and investigated the crystal structures of two new compounds: 2,5-dimethylanilinium tin iodide organic-inorganic hybrid and 2,5-dimethylanilinium triiodide. Starting from 2,5-dimethylaniline and SnI_2, we have investigated the experimental conditions that drive the formation of the hybrid and the triiodide salt. Our findings reveal that the hybrid only grows at elevated temperatures, under inert atmosphere and with the addition of hypophosphorous acid, H_3PO_2. Leaving out any of these three conditions prevents the formation of any product or yields an alternative compound. Crucial for the growth of the triiodide salt is the absence of inert atmosphere. As HI is not very stable in air, the iodide ions, I^-, can easily oxidize to iodine, I_2. This happens in the presence of ambient air and in the absence of any reducing agent, such as H_3PO_2. As a result, a significant amount of I_2 will be formed, which can react with I^- to form the reactive triiodide anion: I_3^-. This triiodide ion then easily reacts with the organic moiety to form the triiodide salt. The affinity between the organic and inorganic groups is therefore an essential design motif for organic-inorganic hybrid structures. Our result shows an alternative structural motif for organic-inorganic hybrids with structural formula ABX_3. Pulse-radiolysis time-resolved microwave conductivity measurements and density functional theory calculations reveal that both compounds have low charge carrier mobilities and very long lifetimes, consistent with their low-dimensional structural characteristics. Our findings add to the understanding of how experimental conditions drive the formation of tin-based organic-inorganic hybrid compounds and how their crystal structures relate to their charge carrier mobilities.

Associated content

Crystallographic information files of the new 2,5-DMAI$_3$ and 2,5-DMASnI$_3$ compounds (CIF). The CIFs is also deposited to the CCDC and are available under the numbers 1839245 and 1839247, respectively.

Acknowledgements

MEK was supported by the Netherlands Organisation for Scientific Research NWO (Graduate Programme 2013, no. 022.005.006). We

thank H.-H. Fang for the absorption measurements and S. Faraji for stimulating discussions.

Appendix A. Supplementary material

Supplementary data associated with this article can be found in the online version at doi:10.1016/j.jssc.2018.12.029.

References

[1] G.C. Papavassiliou, Synthetic three- and lower-dimensional semiconductors based on inorganic units, Mol. Cryst. Liq. Cryst. 286 (1996) 231–238.
[2] D.B. Mitzi, Synthesis, crystal structure, and optical and thermal properties of $(C4H_9N_H3)_2M_I4$ (M = Ge, Sn, Pb), Chem. Mater. 8 (1996) 791–800.
[3] K. Tanaka, T. Takahashi, T. Ban, T. Kondo, K. Uchida, N. Miura, Comparative study on the excitons in lead-halide-based perovskite-type crystals $CH3_NH3_PbBr3$ $CH3_NH3_PbI3$, Solid State Commun. 127 (2003) 619–623.
[4] H.-H. Fang, R. Raissa, M. Abdu-Aguye, S. Adjokatse, G.R. Blake, J. Even, M.A. Loi, Photophysics of organic-inorganic hybrid lead iodide perovskite single crystals, Adv. Funct. Mater. 25 (2015) 2378–2385.
[5] J. Mizusaki, K. Arai, K. Fueki, Ionic conduction of the perovskite-type halides, Solid State Ion. 11 (1983) 203–211.
[6] D.B. Mitzi, S. Wang, C.A. Feild, C.A. Chess, A.M. Guloy, N. Series, Conducting layered organic-inorganic halides containing < 110 > -oriented perovskite sheets, Science 267 (1995) 1473–1476.
[7] Z.-K. Tan, R.S. Moghaddam, M.L. Lai, P. Docampo, R. Higler, F. Deschler, M. Price, A. Sadhanala, L.M. Pazos, D. Credgington, et al., Bright light-emitting diodes based on organometal halide perovskite, Nat. Nanotechnol. 9 (2014) 687–692.
[8] F. Zhang, H. Zhong, C. Chen, X. Wu, X. Hu, H. Huang, Brightly luminescent and color-tunable colloidal $CH3_NH3_PbX3$ (X = Br , I , Cl) quantum dots: potential alternatives for display technology, ACS Nano 9 (2015) 4533–4542.
[9] G. Xing, N. Mathews, S.S. Lim, N. Yantara, X. Liu, D. Sabba, M. Grätzel, S. Mhaisalkar, T.C. Sum, Low-temperature solution-processed wavelength-tunable perovskites for lasing, Nat. Mater. 13 (2014) 476–480.
[10] Y. Zhao, K. Zhu, Organic-inorganic hybrid lead halide perovskies for optoelectronic and electronic applications, Chem. Soc. Rev. 45 (2016) 655–689.
[11] Y. Fang, Q. Dong, Y. Shao, Y. Yuan, J. Huang, Highly narrowband perovskite single-crystal photodetectors enabled by surface-charge recombination, Nat. Photonics 9 (2015) 679–686.
[12] Q. Chen, H. Zhou, Z. Hong, S. Luo, H.-S. Duan, H.-H. Wang, Y. Liu, G. Li, Y. Yang, Planar heterojunction perovskite solar cells via vapor assisted solution process, J. Am. Chem. Soc. 136 (2014) 622–625.
[13] D. Liu, T.L. Kelly, Perovskite solar cells with a planar heterojunction structure prepared using room-temperature solution processing techniques, Nat. Photonics 8 (2013) 133–138.
[14] M. Liu, M.B. Johnston, H.J. Snaith, Efficient planar heterojunction perovskite solar cells by vapour deposition, Nature 501 (2013) 395–398.
[15] W. Ke, G. Fang, J. Wan, H. Tao, Q. Liu, L. Xiong, P. Qin, J. Wang, H. Lei, G. Yang, et al., Efficient hole-blocking layer-free planar halide perovskite thin-film solar cells, Nat. Commun. 6 (2015) 6700.
[16] W. Zhang, M. Saliba, D.T. Moore, S.K. Pathak, M.T. Hörantner, T. Stergiopoulos, S.D. Stranks, G.E. Eperon, J.A. Alexander-Webber, A. Abate, et al., Ultrasmooth organic–inorganic perovskite thin-film formation and crystallization for efficient planar heterojunction solar cells, Nat. Commun. 6 (2015) 6142.
[17] L. Patrick, Lead toxicity, a review of the literature. Part I: exposure, evaluation, and treatment, Altern. Med. Rev. 11 (2006) 2–22.
[18] N.K. Noel, S.D. Stranks, A. Abate, C. Wehrenfennig, S. Guarnera, A.-A. Haghighirad, A. Sadhanala, G.E. Eperon, S.K. Pathak, M.B. Johnston, et al., Lead-free organic-inorganic tin halide perovskites for photovoltaic applications, Energy Environ. Sci. 7 (2014) 3061–3068.
[19] F. Hao, C.C. Stoumpos, D.H. Cao, R.P.H. Chang, M.G. Kanatzidis, Lead-free solid-state organic–inorganic halide perovskite solar cells, Nat. Photonics 8 (2014) 489–494.
[20] C.C. Stoumpos, C.D. Malliakas, M.G. Kanatzidis, Semiconducting tin and lead iodide perovskites with organic cations: phase transitions, high mobilities, and near-infrared photoluminescent properties, Inorg. Chem. 52 (2013) 9019–9038.
[21] Y. Dang, Y. Zhou, X. Liu, D. Ju, S. Xia, H. Xia, X. Tao, Formation of hybrid perovskite tin iodide single crystals by top-seeded solution growth, Angew. Chem. Int. Ed. 55 (2016) 3447–3450.
[22] C.R. Kagan, D.B. Mitzi, C.D. Dimitrakopoulos, Organic-inorganic hybrid materials as semiconducting channels in thin-film field-effect transistors, Science 286 (1999) 945–948.
[23] Y. Takahashi, R. Obara, Z.-Z. Lin, Y. Takahashi, T. Naito, T. Inabe, S. Ishibashi, K. Terakura, Charge-transport in tin-iodide perovskite $CH_3NH_3SnI_3$: origin of high conductivity, Dalton Trans. 40 (2011) 5563–5568.
[24] D.B. Mitzi, C.A. Feild, Z. Schlesinger, R.B. Laibowitz, Transport, optical, and magnetic properties of the conducting halide perovskite $CH_3NH_3SnI_3$, J. Solid State Chem. 114 (1995) 159–163.
[25] C.C. Stoumpos, L. Mao, C.D. Malliakas, M.G. Kanatzidis, Structure-band gap relationships in hexagonal polytypes and low- dimensional structures of hybrid tin iodide perovskites, Inorg. Chem. 56 (2017) 56–73.
[26] D.B. Mitzi, A layered solution crystal growth technique and the crystal structure of $(C_6H_5C_2H_4NH_3)_2PbCl_4$, J. Solid State Chem. 704 (1999) 694–704.
[27] G.M. Sheldrick, SHELXL97, Program for Crystal Structure Refinement, University of Göttingen, Germany, 1997.
[28] P.E. Blöchl, Projector augmented-wave method, Phys. Rev. B 50 (1994) 17953–17979.
[29] G. Kresse, D. Joubert, From ultrasoft pseudopotentials to the projector augmented-wave method, Phys. Rev. B 59 (1999) 1758–1775.
[30] S. Grimme, J. Antony, S. Ehrlich, H. Krieg, A consistent and accurate ab initio parametrization of density functional dispersion correction (DFT-D) for the 94 elements H-Pu, J. Chem. Phys. 132 (2010) 154104.
[31] J.P. Perdew, K. Burke, M. Ernzerhof, Generalized gradient approximation made simple, Phys. Rev. Lett. 77 (18) (1996) 3865–3868.
[32] J.P. Perdew, K. Burke, M. Ernzerhof, Generalized gradient approximation made simple, Phys. Rev. Lett. 78 (1997) 1396.
[33] M.E. Kamminga, G.A. De Wijs, R.W.A. Havenith, G.R. Blake, T.T.M. Palstra, The role of connectivity on electronic properties of lead iodide perovskite-derived compounds, Inorg. Chem. 56 (2017) 8408–8414.
[34] K. Murata, M. Tokumoto, H. Amzai, H. Bando, G. Saito, K. Kajimura, T. Ishiguro, Superconductivity with the onset at 8 K in the organic conductor β-(BEDT-TTF)2_I3, J. Phys. Soc. Jpn. 54 (1985) 1236–1239.
[35] R.P. Shibaeva, V.F. Kaminskii, V.K. Bel'skii, Crystal structure of the organic superconductor Bis-(ethylenedithiolo)tetrathiafulvalene triiodide, (BEDT-TTF)2_I3, Kristallografiya 29 (1984) 1089–1093.
[36] A. Merkys, A. Vaitkus, J. Butkus, M. Okulič-Kazarinas, V. Kairys, S. Gražulis, COD::cif::parser: an error-correcting cif parser for the perl language, J. Appl. Cryst. 49 (2016) 292–301.
[37] S. Gražulis, A. Merkys, A. Vaitkus, M. Okulič-Kazarinas, Computing stoichiometric molecular composition from crystal structures, J. Appl. Cryst. 48 (2015) 85–91.
[38] S. Gražulis, A. Daškevič, A. Merkys, D. Chateigner, L. Lutterotti, M. Quirós, N.R. Serebryanaya, P. Moeck, R.T. Downs, A. Le Bail, Crystallography open database (COD): an open-access collection of crystal structures and platform for world-wide collaboration, Nucleic Acids Res. 40 (2012) D420–D427.
[39] S. Gražulis, D. Chateigner, R.T. Downs, A.F.T. Yokochi, M. Quirós, L. Lutterotti, E. Manakova, J. Butkus, P. Moeck, A. Le Bail, Crystallography open database – an open-access collection of crystal structures, J. Appl. Cryst. 42 (2009) 726–729.
[40] R.T. Downs, M. Hall-Wallace, The american mineralogist crystal structure database, Am. Miner. 88 (2003) 247–250.
[41] E. Fialho De Assis, R.A. Howie, J.L. Wardell, 2-(2-Pyridyl)pyridinium triiodide, Acta Cryst. C52 (1996) 955–957.
[42] S. Christie, R.H. Dubois, R.D. Roger, P.S. White, M.J. Zaworotko, Air stable liquid clathrates: solid state structure and hydrocarbon solubility of organic cation triiodide salts, J. Incl. Phenom. Mol. Recognit. Chem. 11 (1991) 103–114.
[43] J. Janczak, Y.M. Idemori, [Phthalocyaninato(2-)]arsenic(III) triiodide, Acta Cryst. E58 (2002) m36–m38.
[44] A.J. Blake, C. Caltagirone, V. Lippolis, M. Schröder, C. Wilson, (Ferrocenylmethyl) trimethylammonium triiodide, Acta Cryst. E60 (2004) m20–m21.
[45] G.J. Reiss, P.B. Leske, 2-aminopyridin-1-ium triiodide, Acta Cryst. E69 (2013) o1060–o1061.
[46] H.-K. Fun, K. Chanawanno, S. Chantrapromma, (*E*)-2-[4-(dimethylamino)styryl]-1-methylpyridinium triiodide, Acta Cryst. E67 (2011) o2151.
[47] A. Kochel, 4-(4-Pyridyl)pyridinium triiodide, Acta Cryst. E62 (2006) o5605–o5606.
[48] X. Tan, S. Sun, W. Yu, D. Xing, Y. Wang, C. Qi, Trans-4-[P-(N,N-diethylamino) styryl]-N-methyl-pyridinium triiodide, Acta Cryst. E60 (2004) o1054–o1056.
[49] H. He, A.G. Sykes, 4-tert-butylpyridinium triiodide-4-tert-butylpyridine, Acta Cryst. E56 (2011) o434.
[50] M.I. Ikhile, M.D. Bala, 1,3-bis(2,6-diisopropylphenyl)-4,5-dihydro-1H-imidazol-3-ium triiodide, Acta Cryst. E66 (2010) o3121.
[51] X.-J. Tan, S.-X. Sun, S.-L. Liu, J.-P. Ma, D.-X. Xing, 1,4-dimethylpyridinium triiodide, Acta Cryst. E61 (2005) o756–o757.
[52] T.W. Hambley, T.W. Jackson, M. Kojima, R.B. Knott, R.M. Lambrecht, P. Turner, 6,6,9,9-tetramethyl-1,2,5,6,9,9a-hexahydroimidazo[2,1-d][1,2,5]dithiazepin-1-ium triiodide, Acta Cryst. E57 (2001) 0315–0317.
[53] G.J. Gainsford, T. Kemmitt, Dihydrobis(methylamine)borate triiodide, Acta Cryst. C62 (2006) o602–o604.
[54] S. Oberparleiter, G. Laus, K. Wurst, H. Schottenberger, 1,2,3,5-tetramethyl-1H-pyrazol-2-ium triiodide, IUCrData 1 (2016) x161331.
[55] B.F. Ali, R. Al-Far, S.F. Haddad, Crystal supramolecularity of organic-inorganic hybrids of polyhalides: structures of 2 ,5-dibromopyrazinium triiodide and 2-bromopyridinium dibromoiodide, Main Group Chem. 8 (2009) 177–187.
[56] W. Zhang, S. Pathak, N. Sakai, T. Stergiopoulos, P.K. Nayak, N.K. Noel, A.A. Haghighirad, V.M. Burlakov, D.W. DeQuilettes, A. Sadhanala, et al., Enhanced optoelectronic quality of perovskite thin films with hypophosphorous acid for planar heterojunction solar cells, Nat. Commun. 6 (2015) 10030.
[57] M.C. Gélvez-Rueda, E.M. Hutter, D.H. Cao, N. Renaud, C.C. Stoumpos, J.T. Hupp, T.J. Savenije, M.G. Kanatzidis, F.C. Grozema, Interconversion between free charges and bound excitons in 2D hybrid lead halide perovskites, J. Phys. Chem. C 121 (2017) 26566–26574.
[58] M.C. Gélvez-Rueda, N. Renaud, F.C. Grozema, Temperature dependent charge carrier dynamics in formamidinium lead iodide perovskite, J. Phys. Chem. C 121 (2017) 23392–23397.
[59] M.C. Gélvez-Rueda, D.H. Cao, S. Patwardhan, N. Renaud, C.C. Stoumpos, G.C. Schatz, J.T. Hupp, O.K. Farha, T.J. Savenije, M.G. Kanatzidis, et al., Effect of cation rotation on charge dynamics in hybrid lead halide perovskites, J. Phys. Chem. C 120 (2016) 16577–16585.
[60] J.M. Warman, G.H. Gelinck, M.P. De Haas, The mobility and relaxation kinetics of charge carriers in molecular materials studied by means of pulse-radiolysis time-resolved microwave conductivity: dialkoxy-substituted phenylene- vinylene polymers, J. Phys. Condens. Matter 14 (2002) 9935–9954.
[61] J.M. Warman, M.P. De Haas, G. Dicker, F.C. Grozema, J. Piris, M.G. Debije, Charge mobilities in organic semiconducting materials determined by pulse-radiolysis time-resolved microwave conductivity: π-bond-conjugated polymers versus π-π-stacked discotics, Chem. Mater. 16 (2004) 4600–4609.